Available online at www.sciencedirect.com
ScienceDirect
Trans. Nonferrous Met. Soc. China 35(2025) 2135−2147
Transactions of Nonferrous Metals Society of China
www.tnmsc.cn

Role of Sr and Mn alloying on microstructure and comprehensive performance in as-cast Al−Si−Fe−Mg−Cu alloy

Shuan-cheng MENG[1,2], Li YANG[1], Min-qiang GAO[1,3], Jun-wen LI[1], Ren-guo GUAN[1,3]

1. Key Laboratory of Near-Net Forming of Light Metals of Liaoning Province, Dalian Jiaotong University, Dalian 116028, China;
2. School of Materials Science and Engineering, Northeastern University, Shenyang 110819, China;
3. Engineering Research Center of Continuous Extrusion, Ministry of Education, Dalian Jiaotong University, Dalian 116028, China

Received 11 November 2023; accepted 16 May 2024

Abstract: To fabricate Al−Si−Fe−Mg−Cu alloys with superior comprehensive performances, Sr and Mn elements were used to modify secondary phases, i.e., eutectic Si and Fe-rich phases. As the Sr element content increases from 0 to 0.02 wt.%, the morphology of eutectic Si phases changes from coarse lamellar to fine fibrous. However, due to the increased porosity caused by Sr, the mechanical properties and thermal conductivity of the as-cast alloy with Sr content of 0.03 wt.% are weakened. Under the optimized Sr content, Mn element was added to further tailor the properties of the as-cast alloy. With the increase in Mn content from 0.2 to 0.6 wt.%, the needle-like β-Al_5FeSi phases transform into Chinese-script α-$Al_{15}(Fe,Mn)_3Si_2$ phases, and the mechanical properties of the alloy are initially enhanced, then weakened. The thermal conductivity is decreased owing to the solution of Mn atoms in the alloy. In comparison, Al−Si−Fe−Mg−Cu alloy with addition of 0.02 wt.% Sr and 0.4 wt.% Mn exhibits a satisfactory comprehensive performance, with thermal conductivity of 168.5 W/(m·K), ultimate tensile strength of 201.9 MPa, yield strength of 115.3 MPa, and elongation of 9.0%.

Key words: Al−Si alloy; modification treatment; secondary phases; mechanical properties; thermal conductivity

1 Introduction

Al−Si−Fe alloys are broadly utilized in automotive, aerospace, and communication fields due to their low density, high specific strength, and castability [1−4]. The focus has been turned on improvements in mechanical properties and thermal conductivity of the Al−Si−Fe alloys. The demand for the combination of mechanical properties and thermal conductivity of alloys has increased. Therefore, the research on Al−Si−Fe alloys with excellent performances has a significant engineering and application value.

Extensive studies have been carried out on the mechanical properties and thermal conductivity of Al−Si−Fe alloys. Fe elements tend to form brittle secondary phases with Si elements due to their low solid solubility in α(Al), which deteriorates the mechanical properties [5]. SONG et al [6] reported that a gravity-cast Al−7Si−1.2Fe alloy possessed a tensile strength of only 175 MPa and elongation within 2%, which was related to the formation of needle-like β-Al_5FeSi phases. In addition, the thermal conductivities of as-cast ADC12 and A380 alloys were smaller than 110 W/(m·K) owing to the unmodified coarse eutectic Si phases [7]. CHEN et al [8] reported that the thermal conductivities of

Corresponding author: Min-qiang GAO, Tel: +86-411-84109275, E-mail: mqgao@djtu.edu.cn;
Ren-guo GUAN, Tel: +86-411-84106382, E-mail: guanrenguo@sina.cn
https://doi.org/10.1016/S1003-6326(25)66805-1

gravity-cast and die-cast Al−Si−Fe−Cu−Zn alloys were 143 and 126 W/(m·K), respectively. After T4 heat treatment, due to the occurrence of spheroidized Si phases, the thermal conductivity of the die-cast Al−Si−Fe−Cu−Zn alloy reached 151 W/(m·K). QIN et al [9] reported an as-cast Al−8Si−0.1Cu−0.6Mg−0.7Fe−0.6V alloy with tensile strength of 225.6 MPa and thermal conductivity of 132.2 W/(m·K). The comprehensive properties of as-cast Al−Si−Fe alloys are still unsatisfactory. There is often a contradictory relationship between mechanical properties and thermal conductivity of Al alloys, i.e., an increasing strength accompanied by a decreasing thermal conductivity [10]. There are no extensive studies on enhancements in comprehensive performances of Al−Si−Fe alloys.

Alloying has an important role in the determination of microstructures and properties of Al alloys [11]. For example, LIU et al [12] reported that Mg and Cu elements refined the secondary dendrite arm spacing (SDAS) owing to constitutional supercooling, thus enhancing the mechanical properties of the Al−Si−Fe alloy. GAN et al [13] reported that Sr element addition caused a change in eutectic Si phases from a needle morphology to a fibrous morphology, which was beneficial for an increased thermal conductivity. In addition, the Fe element effectively improves the demolding ability for die casting [5]. However, the Fe elements tend to form the needle β-Al_5FeSi phases in Al−Si−Fe alloys, which increases the stress concentration and weakens the mechanical properties of the alloy [14]. GAO et al [15] and EIDHED [16] reported that Mn and Cr elements modified β-Al_5FeSi phases, and enhanced the mechanical properties of the alloys. Moreover, ZHOU et al [7] reported that Mn element had a small effect on the thermal conductivity in comparison to Cr element. QIN et al [9] developed an as-cast Al−Si−Fe−Mg−Cu alloy with a tensile strength of 195.4 MPa and thermal conductivity of 172.7 W/(m·K). Therefore, based on the alloying concept, further improvements in mechanical properties and thermal conductivity of Al−Si−Fe alloys are necessary.

In this study, an as-cast Al−Si−Fe−Mg−Cu−Mn−Sr alloy with a good comprehensive performance was fabricated. The effects of Sr and Mn contents on the microstructure, mechanical properties, and thermal conductivity of Al−Si−Fe−Mg−Cu alloys were investigated. Furthermore, the corresponding mechanisms for microstructure evolution and performance improvement were revealed. The aim of this study was to obtain high-performance as-cast Al−Si−Fe alloys via alloying.

2 Experimental

Pure Al (99.99 wt.%), Al−30wt.%Si, Al−10wt.%Fe, Al−20wt.%Mg, Al−50wt.%Cu, Al−10wt.%Sr, and Al−20wt.%Mn master alloys were used to prepare the Al−Si−Fe−Mg−Cu alloys with various Sr and Mn contents. The alloys were melted in a clay-graphite crucible using a resistance furnace at 750 °C. As the melt temperature decreased to 720 °C, degassing and deslagging were performed. The melt was then poured into a mold to form the ingots. The chemical compositions of the alloys were determined by an inductively coupled plasma-optical emission spectrometer (ICP-OES, PerkinElmer Avio200, USA). The actual compositions of the as-cast alloys are listed in Table 1. Schematics of the mold and sampling position for the microstructure observation and performance testing are shown in Fig. 1.

Table 1 Actual compositions of designed as-cast alloys (wt.%)

Alloy	Si	Fe	Mg	Cu	Mn	Sr	Al
0Mn-0Sr	8.08	0.43	0.56	0.15	0.00	0.00	Bal.
0Mn-1Sr	8.20	0.42	0.56	0.15	0.00	0.01	Bal.
0Mn-2Sr	7.97	0.42	0.58	0.17	0.00	0.02	Bal.
0Mn-3Sr	7.92	0.44	0.59	0.15	0.00	0.03	Bal.
2Mn-2Sr	8.12	0.43	0.57	0.16	0.22	0.02	Bal.
4Mn-2Sr	8.21	0.45	0.55	0.18	0.39	0.02	Bal.
6Mn-2Sr	7.86	0.45	0.55	0.14	0.61	0.02	Bal.

The specimens for microstructure observation were etched using a Keller's agent for 12 s after grinding and polishing. To further observe the morphology of eutectic Si phases after modification, deep etching was conducted using a solution of 10 vol.% HCl and 90 vol.% ethanol for 40 min. The microstructure was observed by optical microscopy (OM, Leica DMi8A, Germany) and scanning electron microscopy (SEM, Zeiss Ultra Plus, Germany) equipped with energy-dispersive spectroscopy (EDS). The second dendritic arm spacing

(SDAS) was measured by the linear intercept method [17]. The crystallography of the phases was analyzed using transmission electron microscopy (TEM, JEM 2100F, Japan). Thin foils having a diameter of 3 mm and height of 30 μm for TEM observation were prepared by ion milling using a Gatan 695 precision ion polishing system.

Tensile tests were carried out at a strain rate of $1\times10^{-3}\ s^{-1}$ using an electronic universal tensile machine (UTM, CMT5305, China) at a room temperature of 25 °C. The fracture surfaces of tensile specimens were analyzed by SEM. The thermal conductivities of the specimens were determined by a laser flash diffusivity instrument (FLD, NETZSCH LFA 427, Germany), and calculated by [12]

$$\lambda=\alpha\rho c_p \quad (1)$$

where α is the thermal diffusivity, ρ is the density and c_p is the specific heat capacity. Moreover, the electrical conductivity was measured using a digital electrical instrument (Fischer SMP350, Germany). To ensure reliability of the experimental data, each sample was measured at least three times, and the average value was presented.

3 Results

3.1 Effect of Sr element on microstructure

Figure 2 shows the microstructures of the 0Mn-0Sr, 0Mn-1Sr, 0Mn-2Sr and 0Mn-3Sr alloys. The microstructures of the alloys consist of α(Al)

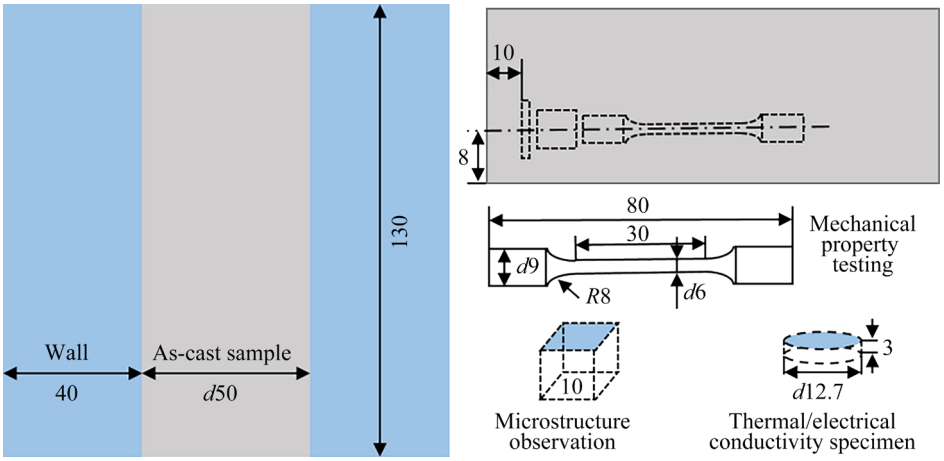

Fig. 1 Schematics showing mold and sampling position for microstructure observation and performance testing (Unit: mm)

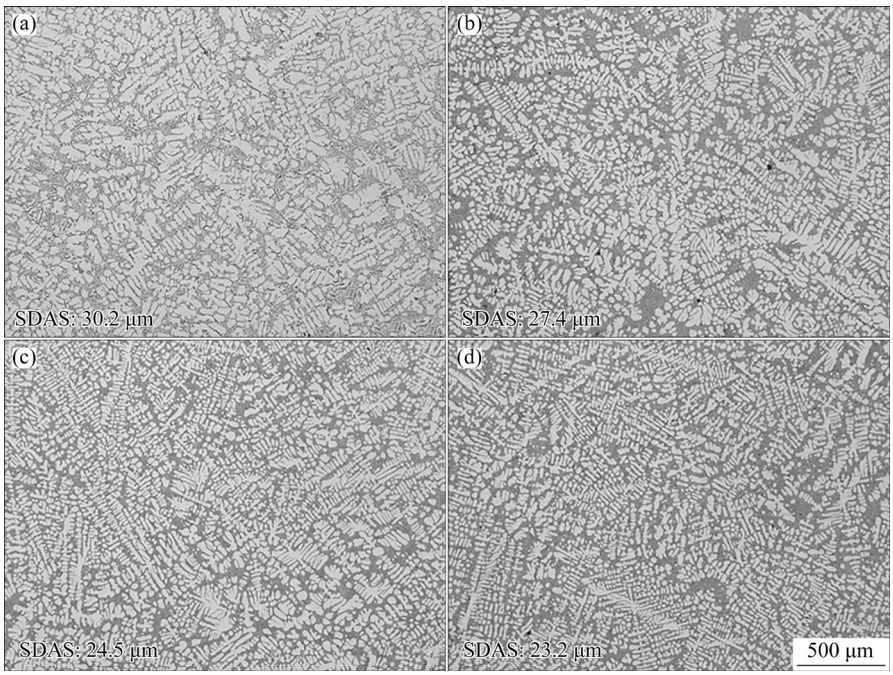

Fig. 2 OM images of Al−Si−Fe−Mg−Cu alloys with various Sr contents: (a) 0 wt.%; (b) 0.01 wt.%; (c) 0.02 wt.%; (d) 0.03 wt.%

dendrites and secondary phases. Furthermore, with the increase in the Sr content from 0 to 0.03 wt.%, the SDAS decreases from 30.2 to 23.2 μm.

Secondary phases are observed by SEM, as shown in Fig. 3. When the Sr content is 0 wt.%, secondary phases are composed of gray and white phases with a needle morphology, as shown in Fig. 3(a). With the increase in the Sr content from 0 to 0.03 wt.%, the eutectic Si phases exhibit a fibrous morphology, while the Fe-rich phases do not change, as shown in Figs. 3(b–d). The EDS result for Point A in Fig. 3(c) shows that the gray phase consists of Al, Si, and Sr elements, as shown in Fig. 3(e). Al, Fe, and Si elements form the white phase (Point B in Fig. 3(c)), as shown in Fig. 3(f). The results indicate that the gray and white phases are eutectic Si and Fe-rich phases, respectively. In addition, when the Sr content is 0.03 wt.%, pores are observed, as shown in Fig. 3(d). The average length of eutectic Si phases decreases with the increase in the Sr content, as shown in Fig. 4. The increase in the Sr content results in an increase in the porosity.

Figure 5 shows the SEM images of eutectic Si phases after deep-etching in the as-cast alloys with various Sr contents. Coarse lamellar eutectic Si phases are observed in the unmodified alloy, as shown in Fig. 5(a). After the addition of 0.01 wt.% Sr, the coarse lamellar eutectic Si phases are modified, with an acicular characteristic, as shown

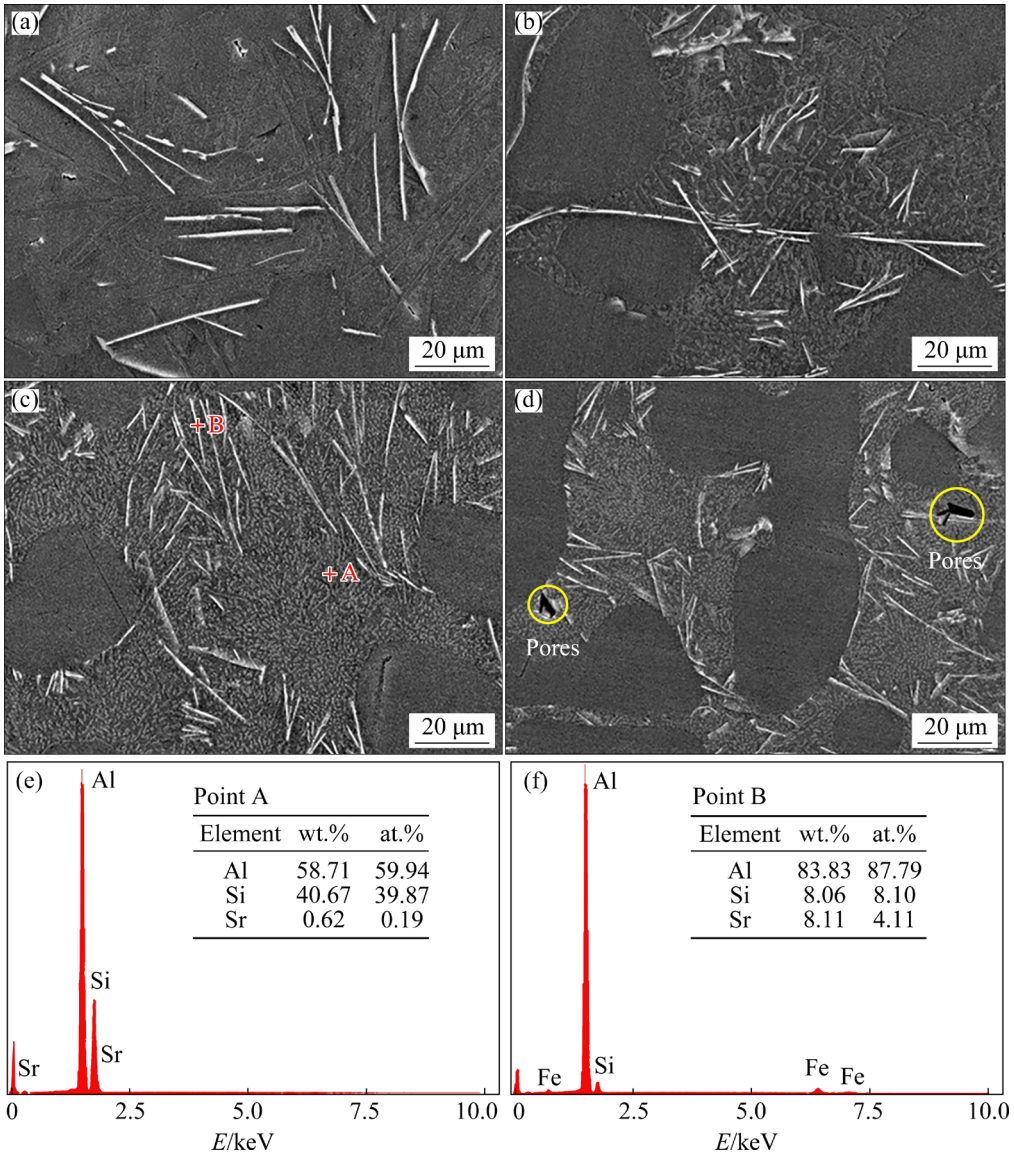

Fig. 3 SEM images of secondary phases in as-cast Al−Si−Fe−Mg−Cu alloys with various Sr additions: (a) 0 wt.%; (b) 0.01 wt.%; (c) 0.02 wt.%; (d) 0.03 wt.%; (e, f) EDS results of eutectic Si and Fe-rich phases marked by Points A and B in (c), respectively

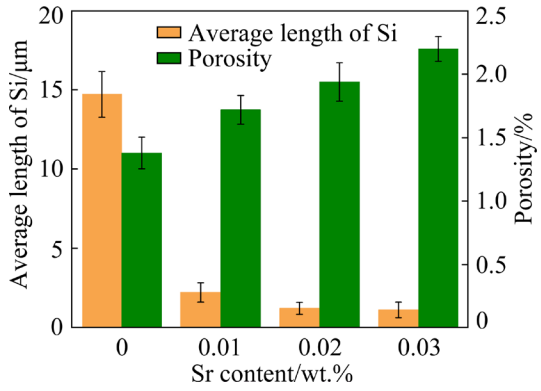

Fig. 4 Average size of eutectic Si phases and porosity in Al−Si−Fe−Mg−Cu alloy after Sr addition

in Fig. 5(b). With the increase in the Sr content to 0.02 and 0.03 wt.%, fine fibrous eutectic Si phases in the alloy are observed, as shown in Figs. 5(c, d).

Figure 6 presents TEM images of the 0Mn-2Sr alloy. A large number of twins and nanometer-sized atom cluster at the edge of twins are observed in the eutectic Si phase, as shown in Fig. 6(a). Figure 6(b) shows the selected area electron diffraction (SAED) pattern of the eutectic Si along the [011] zone axis. The high-resolution TEM (HRTEM) image of the marked area in Fig. 6(a) is presented in Fig. 6(c). The angle of $\{111\}_{Si}$ twins is 109.5°. Furthermore, an atom cluster at the edge of twins is observed. According to the EDS result in Fig. 6(d), the atom cluster consists of Al, Si, and Sr elements, which is consistent with the previous study [18].

3.2 Effect of Mn element on microstructure

Figures 7(a−c) show the OM microstructures of the 2Mn-2Sr, 4Mn-2Sr, and 6Mn-2Sr alloys, respectively. With the increase in the Mn content from 0.2 to 0.6 wt.%, refined dendritic structures are obtained, and the SDAS decreases from 22.3 to 19.3 μm. Fe-rich phases of the 2Mn−2Sr, 4Mn−2Sr and 6Mn−2Sr alloys are found, as shown in Figs. 7(d−f). When the Mn content is 0.2 wt.%, the Fe-rich phases exhibit needle-like or Chinese-script morphologies, as shown in Fig. 7(d).

With the increase in the Mn content to 0.4 wt.%, the needle phases disappear and the number of Chinese-script phases increases, as shown in Fig. 7(e). With the further increase in the Mn content to 0.6 wt.%, large Chinese-script phases are formed, as shown in Fig. 7(f). The EDS result in Fig. 7(g) indicates that the needle-like phase mainly consists of Al, Si, Mn, and Fe elements. A high Mn content is found in the Chinese-script phases and

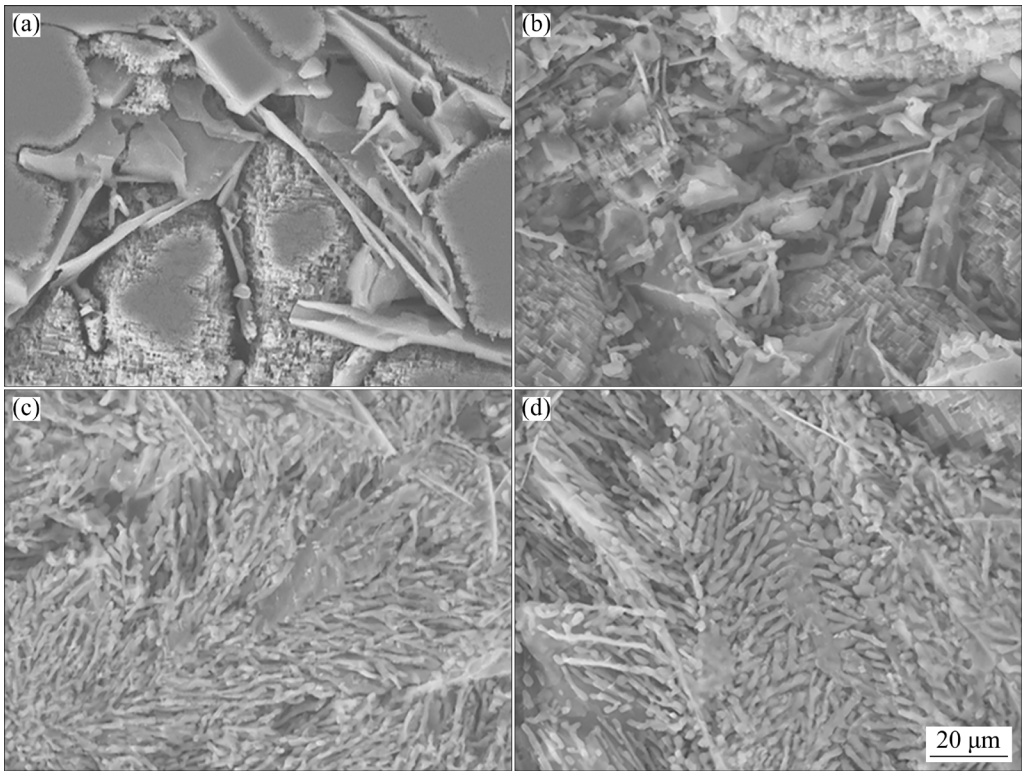

Fig. 5 Morphologies of eutectic Si phases after deep-etching in Al−Si−Fe−Mg−Cu alloys with different Sr contents: (a) 0 wt.%; (b) 0.01 wt.%; (c) 0.02 wt.%; (d) 0.03 wt.%

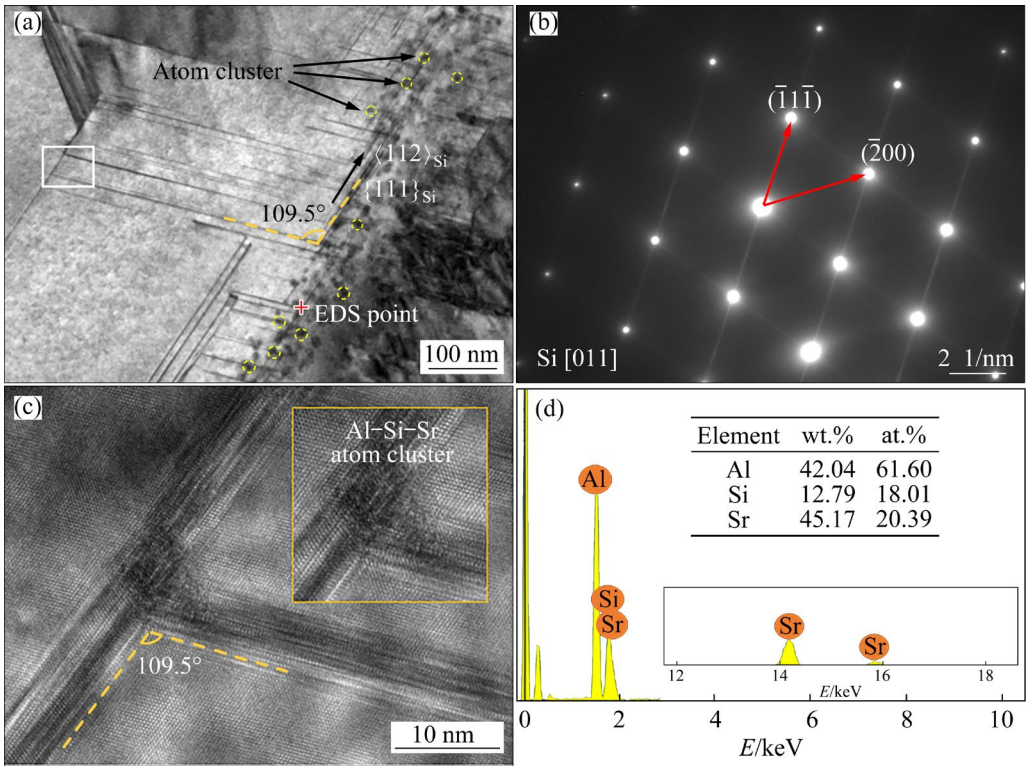

Fig. 6 TEM microstructure of eutectic Si in 0Mn-2Sr alloy: (a) Bright-field image; (b) SAED pattern of eutectic Si; (c) HRTEM image of area marked by rectangle in (a); (d) EDS result of atom cluster in (a)

large phases (13.69 and 15.98 wt.%, respectively), as shown in Figs. 7(h, i). Figure 7(j) shows an SEM image of the 4Mn-2Sr alloy, where Chinese-script Fe-rich phases and fine fibrous eutectic Si phases are observed. The corresponding element mapping results in Fig. 7(k) show that the Sr element is adsorbed on eutectic Si phases. The Mn element has the same distribution as that of the Fe element. In addition, Mg and Cu elements uniformly distribute in the matrix.

To further analyze the Fe-rich phases, the microstructures of the 0Mn-2Sr and 4Mn-2Sr alloys are investigated using TEM, as shown in Fig. 8. A needle-like phase is observed, as shown in Fig. 8(a). The element mapping results in Figs. 8(a_1–a_3) show that the needle-like phase consists of Al, Fe, and Si elements. The corresponding SAED pattern (Fig. 8(a_4)) indicates that the phase is β-Al_5FeSi. The HRTEM image (Fig. 8(a_5)) shows that the interplanar spacing of $(01\bar{7})$ of β-Al_5FeSi is 0.43 nm [6]. The Fe-rich phase is also observed in the 4Mn-2Sr alloy, as shown in Fig. 8(b). The element mapping results in Figs. 8(b_1–b_3) indicate that Si, Fe, and Mn elements are uniformly distributed in the Fe-rich phase. Moreover, the SAED pattern of the Fe-rich phase in 4Mn-2Sr alloy in Fig. 8(b_4) implies that the phase is α-$Al_{15}(Fe,Mn)_3Si_2$ [19]. The HRTEM image in Fig. 8(b_5) demonstrates that the interplanar spacing of $(\bar{1}1\,\bar{1})$ of the α-$Al_{15}(Fe,Mn)_3Si_2$ phase is 0.86 nm.

3.3 Mechanical properties and thermal conductivities

Figure 9(a) shows the engineering stress–strain curves of different alloys. The mechanical properties of alloys are listed in Table 2. With the increase in the Sr content from 0 to 0.03 wt.%, the mechanical properties of the alloy are initially enhanced, and then weakened. When the Sr content is 0.02 wt.%, the mechanical properties of the alloy reach the maximum. The ultimate tensile strength (UTS), yield strength (YS) and elongation (EL) of the alloy with 0.02 wt.% Sr are 182.3 MPa, 89.3 MPa and 6.8%, respectively. In addition, with the increase in the Mn content from 0.2 to 0.6 wt.%, the mechanical properties of the alloy have the same variation tendency as those of the alloys with various Sr contents. The 4Mn-2Sr alloy possesses good mechanical properties, i.e., UTS of 201.9 MPa, YS of 115.3 MPa and EL of 9.0%.

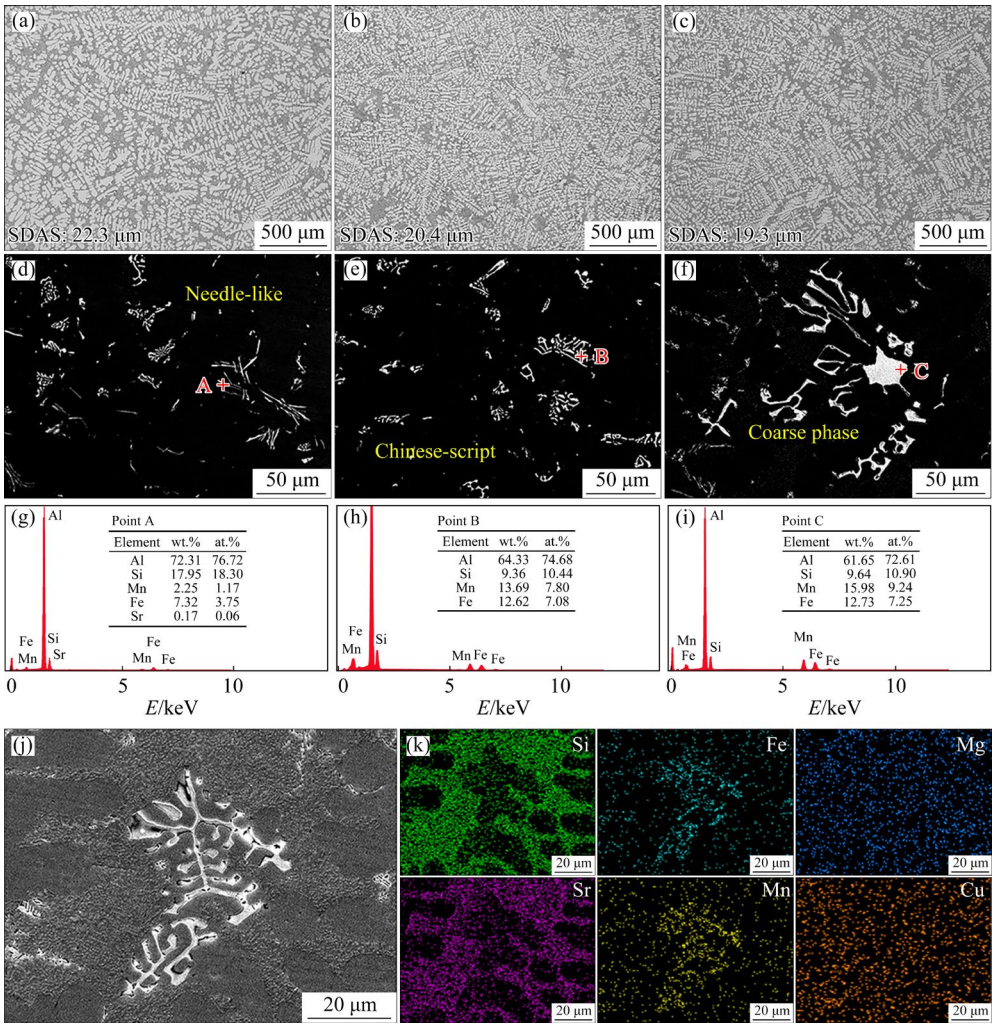

Fig. 7 OM (a−c) and SEM (d−f) images of Al−Si−Fe−Mg−Cu alloys with 0.02 wt.% Sr and different Mn contents: (a, d) 0.2 wt.% Mn; (b, e) 0.4 wt.% Mn; (c, f) 0.6 wt.% Mn; (g−i) Corresponding EDS results of Points A, B, and C, respectively; (j) SEM image of 4Mn−2Sr alloy; (k) Element mapping results for (j)

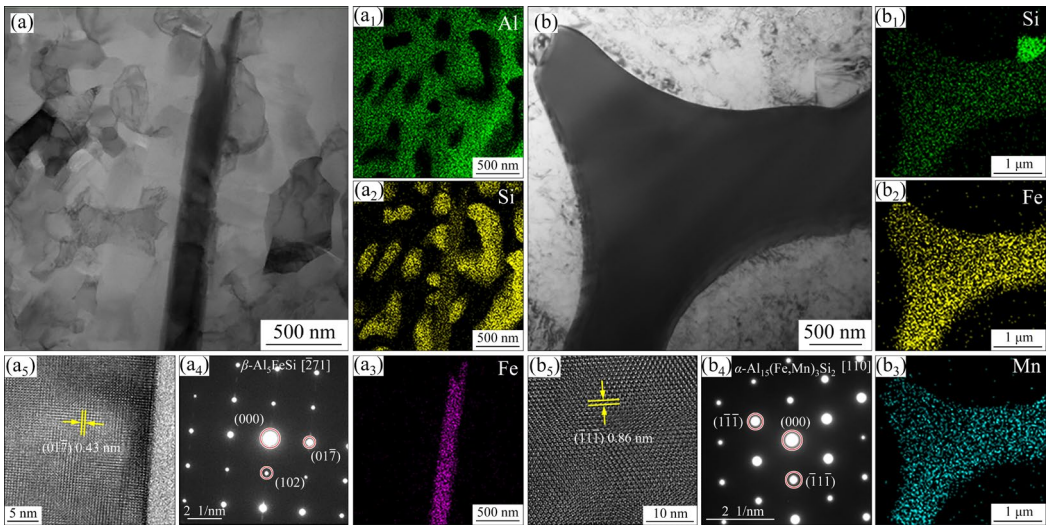

Fig. 8 TEM characterization for 0Mn-2Sr and 4Mn-2Sr alloys: (a) Bright-field image of β-Al_5FeSi phase in 0Mn-2Sr alloy; (a_1–a_3) Element mapping results for (a); (a_4, a_5) SAED pattern and HRTEM image of β-Al_5FeSi phase; (b) Bright-field image of α-$Al_{15}(Fe,Mn)_3Si_2$ phase in 4Mn−2Sr alloy; (b_1–b_3) Element mapping results for (b); (b_4, b_5) SAED pattern and HRTEM image of α-$Al_{15}(Fe,Mn)_3Si_2$ phase

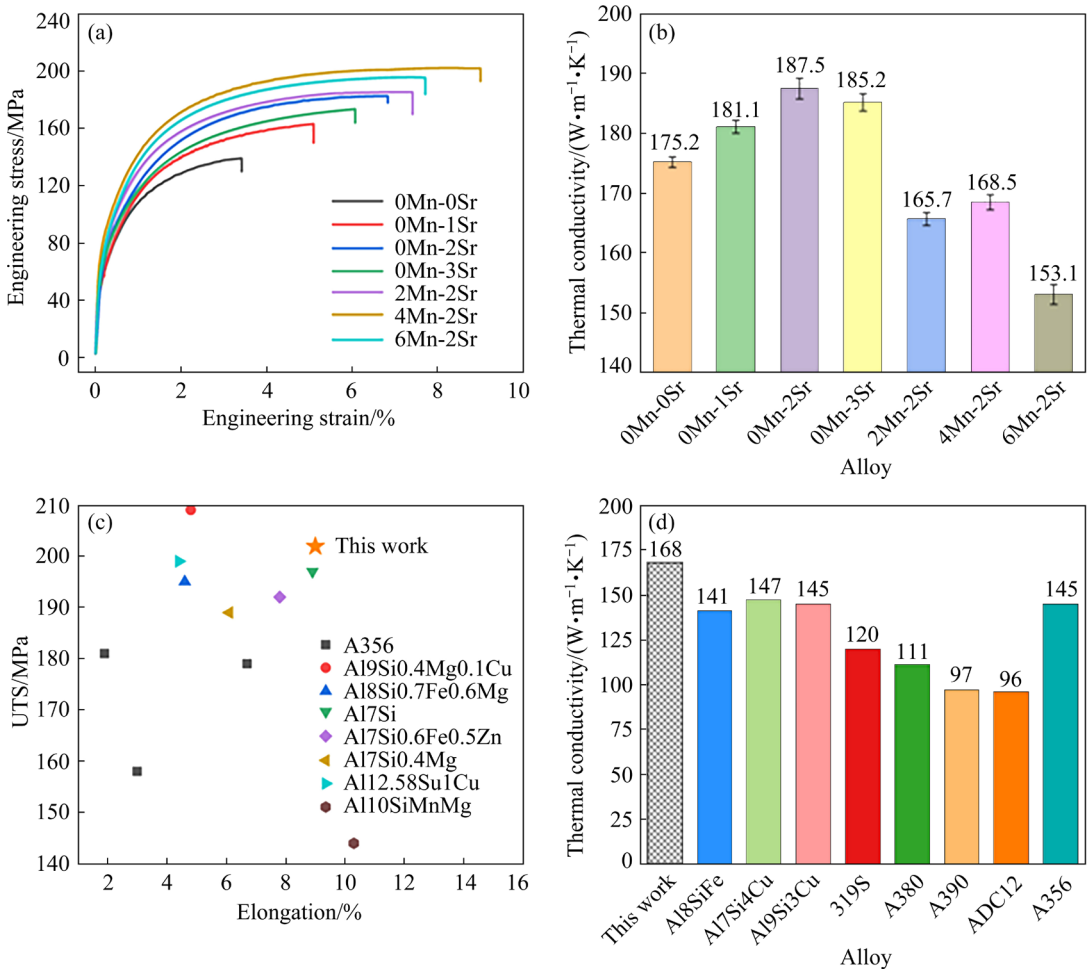

Fig. 9 Engineering stress–strain curves (a) and thermal conductivities (b) of optimized as-cast alloys; Comparison of mechanical properties [9,20−26] (c) and thermal conductivities [5,27−32] (d) with those of other as-cast Al–Si based alloys

Table 2 Mechanical properties of as-cast Al−Si−Fe−Mg−Cu alloys with different Sr and Mn contents

Alloy	UTS/MPa	YS/MPa	EL/%
0Mn-0Sr	139.1±2.4	72.1±5.1	3.4±2.2
0Mn-1Sr	163.1±3.1	76.7±2.4	5.1±1.4
0Mn-2Sr	182.3±3.9	89.3±1.3	6.8±2.7
0Mn-3Sr	173.4±6.5	87.7±2.5	6.1±2.5
2Mn-2Sr	195.3±2.9	102.9±3.4	7.5±1.3
4Mn-2Sr	201.9±3.8	115.3±2.3	9.0±2.2
6Mn-2Sr	185.4±4.3	114.3±2.5	7.4±3.1

Figure 9(b) shows the thermal conductivities of different alloys. The thermal diffusivities, densities and specific heats are listed in Table 3. With the increase in the Sr content from 0 to 0.03 wt.%, the thermal conductivity of the alloy initially increases, and then decreases. When the Sr content is 0.02 wt.%, the thermal conductivity of the alloy reaches the maximum (187.5 W/(m·K)). However, the thermal conductivity significantly decreases with the addition of Mn elements. Notably, an extreme value (168.5 W/(m·K)) appears when the Mn content is 0.4 wt.%. The electrical conductivities of the alloys are summarized in Table 4. The variation tendency of the electrical conductivity is consistent with the thermal conductivity. Therefore, the 4Mn−2Sr alloy is confirmed to be an optimized alloy with good comprehensive properties. Figures 9(c, d) compare the mechanical properties and thermal conductivity of the 4Mn−2Sr alloy fabricated in this study and other as-cast Al–Si alloys. The 4Mn−2Sr alloy possesses a better comprehensive performance.

In addition, the SEM images of the tensile fractographs of the 0Mn-0Sr, 0Mn-2Sr, and 4Mn-2Sr alloys are presented in Fig. 10. Cleavage

Table 3 Thermal conductivities of as-cast Al−Si−Fe− Mg−Cu alloys with various Sr and Mn additions

Alloy	Thermal diffusivity/($mm^2 \cdot s^{-1}$)	Density/ ($g \cdot cm^{-3}$)	Specific heat/($W \cdot g^{-1} \cdot K^{-1}$)	Thermal conductivity/ ($W \cdot m^{-1} \cdot K^{-1}$)
0Mn-0Sr	71.36	2.64	0.93	175.2
0Mn-1Sr	72.48	2.63	0.95	181.1
0Mn-2Sr	75.05	2.63	0.95	187.5
0Mn-3Sr	75.19	2.62	0.94	185.2
2Mn-2Sr	68.45	2.66	0.91	165.7
4Mn-2Sr	69.62	2.66	0.91	168.5
6Mn-2Sr	64.41	2.67	0.89	153.1

Table 4 Electrical conductivities of as-cast Al−Si−Fe− Mg−Cu alloys with different Sr and Mn additions (% (IACS))

0Mn-0Sr	0Mn-1Sr	0Mn-2Sr	0Mn-3Sr	2Mn-2Sr	4Mn-2Sr	6Mn-2Sr
42.67±0.06	44.31±0.09	46.15±0.06	45.42±0.03	38.33±0.04	39.56±0.06	36.86±0.10

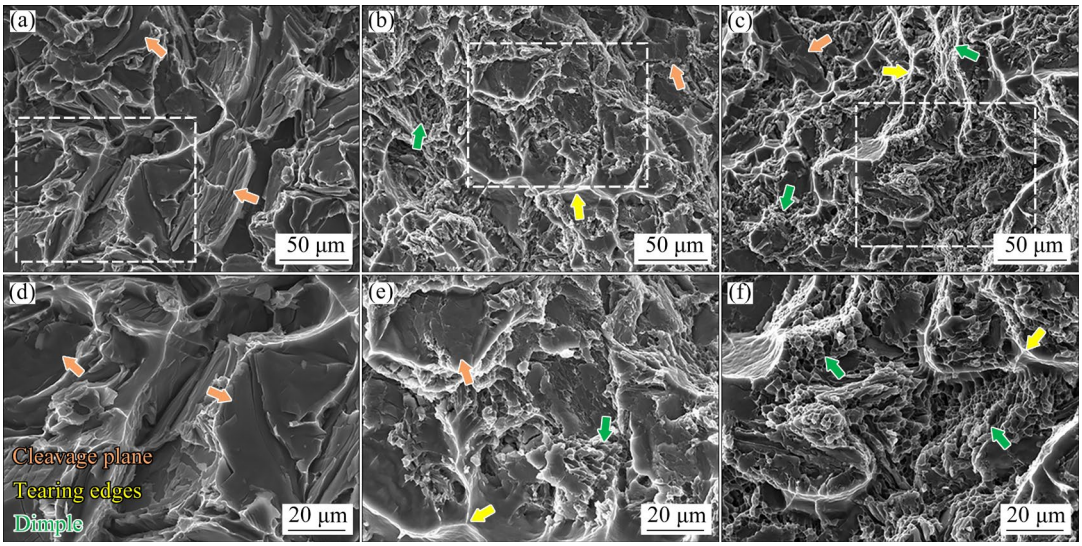

Fig. 10 SEM images of tensile fractographs of as-cast alloys: (a, d) 0Mn-0Sr alloy; (b, e) 0Mn-2Sr alloy; (c, f) 4Mn-2Sr alloy

planes are observed in the 0Mn-0Sr alloy, as shown in Figs. 10(a, d). As the Sr content increases to 0.02 wt.%, the 0Mn-2Sr alloy exhibits an obvious ductile fracture, and some dimples are observed in Figs. 10(b, e). With the further increase in the Mn content to 0.4 wt.%, the area of the cleavage plane considerably decreases, and more dimples are observed, as shown in Figs. 10(c, f). This is consistent with the results of the tensile test on the alloys with various Sr and Mn contents.

4 Discussion

4.1 Microstructure evolution

The SDAS of α(Al) in the as-cast Al−Si−Fe−Mg−Cu alloy is refined because of the enhancement in undercooling caused by alloying elements. The total undercooling (ΔT) of the dendrite tip of the alloy during solidification is expressed as [33]

$$\Delta T=\Delta T_t+\Delta T_c+\Delta T_r \quad (2)$$

where ΔT_t, ΔT_c, and ΔT_r are the thermal undercooling, composition undercooling, and curvature undercooling, respectively. ΔT_t and ΔT_r are assumed to be constants because of the same experimental conditions. The addition of Sr and Mn elements leads to redistribution of solutes at the front of the solid/liquid interface, resulting in an increment in ΔT_c. Therefore, the enhanced ΔT_c promotes nucleation of α(Al), and thus the refined SDAS is obtained.

For secondary phases, the addition of Sr elements results in the formation of fibrous eutectic Si phases due to the twin plane reentrant edge (TPRE) mechanism [34]. Sr atoms are attached to the twin boundaries of two $\{111\}_{Si}$ growth planes to inhibit the optimal growth of Si, which leads to the change in the direction of Si growth, resulting in the high-density twins [35]. In addition, the Mn element modifies the Fe-rich phases from β-Al_5FeSi phases with a needle-like morphology to α-$Al_{15}(Fe,Mn)_3Si_2$ phases with a Chinese-script morphology due to the variation in solidification sequence [36]. The addition of Mn elements increases the solidification temperature of Fe-rich phases (close to or higher than that of the α(Al) phase), which promotes the precipitation and changes the morphology of the Fe-rich phase because of the large growth space. However, the further increase in the Mn content causes the formation of large α-$Al_{15}(Fe,Mn)_3Si_2$ phases due to the excessive nucleation temperature [6].

4.2 Enhanced mechanical properties

After Sr and Mn alloying, there is an obvious increase in strength of the as-cast Al−Si−Fe−Mg−Cu alloys. The yield strength (σ_{ys}) is expressed by [37]

$$\sigma_{ys}=\Delta\sigma_i+\Delta\sigma_{gb}+\Delta\sigma_{eutectic}+\Delta\sigma_{ss}+\Delta\sigma_{ppt} \quad (3)$$

where $\Delta\sigma_i$ is the intrinsic strength, $\Delta\sigma_{gb}$ is the grain boundary strengthening, $\Delta\sigma_{eutectic}$ is the eutectic phases strengthening, $\Delta\sigma_{ss}$ is the solute solution strengthening, and $\Delta\sigma_{ppt}$ is the precipitation hardening. In this study, the alloys without heat treatment possess the same processing parameters, which indicates that $\Delta\sigma_{gb}$ and $\Delta\sigma_{eutectic}$ are major factors. As the contents of Sr and Mn increase, the SDAS of α(Al) grains decreases and the dislocation movement during plastic deformation is hindered by the increased number of dendrite boundaries thus increasing the $\Delta\sigma_{gb}$ [38]. With the increase in the Sr content from 0 to 0.02 wt.%, the size of the eutectic Si phases decreases, which weakens the fragmentation effect of eutectic Si phases on the α(Al) matrix and improves $\Delta\sigma_{eutectic}$ [39,40]. Although the eutectic Si phases of the alloy with 0.03 wt.% Sr are refined, the tendency of hydrogen absorption increases, which increases the crack propagation rate and weakens the mechanical properties [41]. In addition, as the Mn content increases from 0.2 to 0.4 wt.%, the number of β-Al_5FeSi phases decreases and the number of α-$Al_{15}(Fe,Mn)_3Si_2$ phases increases, which weakens the stress concentration and improves the mechanical properties. However, when the Mn content reaches 0.6 wt.%, the formation of large α-$Al_{15}(Fe,Mn)_3Si_2$ phases weakens the mechanical properties of the alloy.

4.3 Improved thermal conductivity

The thermal conductivities of the alloys are related to phonons and electrons. In Al alloys, the electron is a major factor affecting the thermal conductivity, which is attributed to the electron movement [31]. The relationship between the movement of electrons and resistivity (ρ_{total}) is expressed by [12]

$$\rho_{total}=\rho_0+\rho_{SS}+\rho_p+\rho_d+\rho_{gb} \quad (4)$$

where ρ_0 is the basic resistivity of the alloy related to the temperature, and ρ_{SS}, ρ_p, ρ_d, and ρ_{gb} are the resistivities caused by the solution atoms, secondary phase, dislocations and grain boundaries, respectively. In this study, Cu and Mg elements are dissolved in the matrix and do not form phases with other elements. Sr element is adsorbed on Si phases, which indicates that ρ_{SS} is identical in the alloy containing Sr. The effect of ρ_d on the resistivity is ignored at room temperature [13]. The small grain diameter results in an increase in electron scattering and a decrease in thermal conductivity [42]. Therefore, the resistivity caused by secondary phases is a dominant factor affecting the thermal conductivity, which is estimated by [5]

$$\rho_p=\frac{m^* v_F}{n_{ef}e^2}\mu \quad (5)$$

where m^* is the electron mass, v_F is the average velocity of the electron near the Fermi surface, μ is the scattering coefficient, n_{ef} is the number of electrons per unit volume, and e is the electron charge. A smaller μ corresponds to a smaller ρ_p, resulting in an improved thermal conductivity. As the Sr content increases from 0 to 0.02 wt.%, the refined eutectic Si phases are obtained, which decreases μ and improves the thermal conductivity. When the Sr content further increases to 0.03 wt.%, the increased porosity decreases the effective thermal conduction area, leading to a decrease in thermal conductivity [8]. The addition of Mn

elements increases the degree of lattice distortion, which increases ρ_{SS}. The thermal conductivity decreases sharply when the Mn content is 0.2 wt.%. The thermal conductivity is controlled by the Mn solution and the morphology and distribution of Fe-rich phases. The connectivity of Fe-rich phases is weakened owing to the formation of α-$Al_{15}(Fe,Mn)_3Si_2$ phases, which decreases the electron scattering in comparison to β-Al_5FeSi phases. The thermal conductivity increases slightly with the increase in the Mn content from 0.2 to 0.4 wt.%. However, when the Mn content is further increased to 0.6 wt.%, the high content of solid-solution Mn atoms has a detrimental effect on the thermal conductivity due to the lattice distortion, which decreases the thermal conductivity. Therefore, the as-cast Al−Si−Fe−Mg−Cu alloy with the addition of 0.02 wt.% Sr and 0.4 wt.% Mn possesses a good combination of mechanical properties and thermal conductivity.

5 Conclusions

(1) As the Sr content increases from 0 to 0.03 wt.%, the SDAS of α(Al) decreases and the morphology of eutectic Si phases changes from long strips to fine fibers in the as-cast Al−Si−Fe−Mg−Cu alloy.

(2) With the increase in the Mn content from 0.2 to 0.4 wt.%, the needle-like β-Al_5FeSi phases are replaced by α-$Al_{15}(Fe,Mn)_3Si_2$ phases. The further increase in the Mn content leads to the formation of large α-$Al_{15}(Fe,Mn)_3Si_2$ phases.

(3) Owing to the refined SDAS and formation of fine fibrous eutectic Si phases and Chinese-script α-Fe phases, the 4Mn−2Sr alloy possesses an excellent mechanical performance, with UTS of 201.9 MPa, YS of 115.3 MPa, and EL of 9.0%.

(4) Owing to the change in morphology of eutectic Si phases, the 0Mn−2Sr alloy has a superior thermal conductivity of 187.5 W/(m·K), but there is a negative effect on the thermal conductivity due to the lattice distortion caused by solid solution Mn atoms.

CRediT authorship contribution statement

Shuan-cheng MENG: Conceptualization, Formal analysis, Methodology, Data curation, Writing − Original draft; **Li YANG:** Investigation, Validation, Resources; **Min-qiang GAO:** Investigation, Writing − Review & editing, Funding acquisition, Supervision; **Jun-wen LI:** Resources, Methodology, Funding acquisition; **Ren-guo GUAN:** Conceptualization, Project administration, Funding acquisition, Supervision.

Declaration of competing interest

The authors declare that they have no known competing financial interests or personal relationships that could have appeared to influence the work reported in this paper.

Acknowledgments

This work was supported by the National Natural Science Foundation of China (Nos. 52371019, 52301034, and U2341253), and the Open Research Fund of Songshan Lake Materials Laboratory, China (No. 2023SLABFN11).

References

[1] LIN Bo, FAN Tao, LI Hao-yu, ZHAO Yu-liang, ZHANG Wei-wen, LIU Kun. Microstructure and high temperature tensile properties of Al−Si−Cu−Mn−Fe alloys prepared by semi-solid thixoforming [J]. Transactions of Nonferrous Metals Society of China, 2021, 31: 2232−2249.

[2] LI Ke, ZHANG Jin, CHEN Xiao-lin, YIN Yi-hua, HE Yi, ZHOU Zi-qi, GUAN Ren-guo. Microstructure evolution of eutectic Si in Al−7Si binary alloy by heat treatment and its effect on enhancing thermal conductivity [J]. Journal of Materials Research and Technology, 2020, 9: 8780−8786.

[3] WANG Zhen-hong, ZHANG Li-tong, SU Bin, ZHANG Xiao-peng. Simulation on microstructure evolution of Al−Si alloy under effect of natural convection during solidification [J]. Transactions of Nonferrous Metals Society of China, 2022, 32: 79−90.

[4] SAMAT S, OMAR M Z, BAGHADI A H, MOHAMED I F, RAJABI A, AZIZ A M. Microstructural evolution, dislocation density and tensile properties of Al−6.5Si−2.1Cu−0.35Mg alloy produced by different casting processes [J]. Journal of Materials Science & Technology, 2021, 95: 145−157.

[5] QI Ming-fan, KANG Yong-lin, XU Yu-zhao, WULABIEKE Z, LI Jing-yuan. A novel rheological high pressure die-casting process for preparing large thin-walled Al−Si−Fe−Mg−Sr alloy with high heat conductivity, high plasticity and medium strength [J]. Materials Science and Engineering A, 2020, 776: 139040.

[6] SONG Dong-fu, ZHAO Yu-liang, JIA Yi-wang, LI Run-xia, ZHOU Nan, ZHENG Kai-hong, FU Ya-nan, ZHANG Wei-wen. Study of the evolution mechanisms of Fe-rich phases in Al−Si−Fe alloys with Mn modification using synchrotron X-ray imaging [J]. Journal of Alloys and Compounds, 2022, 915: 165378.

[7] ZHOU Yu-li, ZHANG Xun, ZHONG Gu, ZHANG Jun-chao, YANG Yang, KANG Du, LI Hu-tian, JIE Wan-qi,

SCHUMACHER P, LI Jie-hua. Elucidating thermal conductivity mechanism of Al−9Si based alloys with trace transition elements (Mn, Cr, V) [J]. Journal of Alloys and Compounds, 2022, 907: 164446.

[8] CHEN J K, HUNG H Y, WANG C F, TANG N K. Effects of casting and heat treatment processes on the thermal conductivity of an Al−Si−Cu−Fe−Zn alloy [J]. International Journal of Heat and Mass Transfer, 2017, 105: 189−195.

[9] QIN Rong, YAN Rui-Fang, GUAN Zhi-pin, ZHANG Guang-qi, SONG Jia-wang, REN Ming-wen, WANG Jin-guo. Effect of vanadium on Fe-rich phase, mechanical properties and thermal conductivity of hypoeutectic Al−Si alloy [J]. Materials Research Express, 2021, 8: 026518.

[10] DONG Zhong-qiang, WANG Jin-guo, GUAN Zhi-pin, MA Pin-kui, ZHAO Po, LI Zhu-jin, LU Tian-shi, YAN Rui-fang. Effect of short T6 heat treatment on the thermal conductivity and mechanical properties of different casting processes Al−Si−Mg−Cu alloys [J]. Metals, 2021, 11: 1450.

[11] JEONG C Y. Effect of alloying elements on high temperature mechanical properties for piston alloy [J]. Materials Transactions, 2012, 53: 234−239.

[12] LIU Yan, MENG Shuan-cheng, GAO Min-qiang, PAN Shuai, FU Ying, GUAN Ren-guo. Enhanced comprehensive performance via alloying and rheo-diecasting in a semi-solid Al−Si−Fe−Mg−Cu−Sr alloy [J]. Journal of Materials Research and Technology, 2023, 25: 420−439.

[13] GAN Jun-qi, HUANG Yu-jian, WEN Cheng, DU Jun. Effect of Sr modification on microstructure and thermal conductivity of hypoeutectic Al−Si alloys [J]. Transactions of Nonferrous Metals Society of China, 2020, 30: 2879−2890.

[14] TANG Qi, ZHAO Jian-hua, WANG Tao, CHEN Jing, HE Ke. The effects of neodymium addition on the intermetallic microstructure and mechanical properties of Al−7Si−0.3Mg−0.3Fe alloys [J]. Journal of Alloys and Compounds, 2018, 741: 161−173.

[15] GAO Tong, HU Kai-qi, WANG Long-shuai, ZHANG Bang-ran, LIU Xiang-fa. Morphological evolution and strengthening behavior of α-Al(Fe,Mn)Si in Al−6Si−2Fe−xMn alloys [J]. Results in Physics, 2017, 7: 1051−1054.

[16] EIDHED W. Modification of β-Al_5FeSi compound in recycled Al−Si−Fe cast alloy by using Sr, Mg and Cr additions [J]. Journal of Materials Science & Technology, 2008, 24: 45−47.

[17] BERGER A, HERWEGH M, SCHWARZ J O, PUTLITZ B. Quantitative analysis of crystal/grain sizes and their distributions in 2D and 3D [J]. Journal of Structural Geology, 2011, 33: 1751−1763.

[18] LI J H, ALBU M, HOFER F, SCHUMZCHER P. Solute adsorption and entrapment during eutectic Si growth in Al–Si-based alloys [J]. Acta Materialia, 2015, 83: 187−202.

[19] JIAO X Y, LIU C F, GUO Z P, TONG G D, MA S L, BI Y, ZHANG Y F, XIONG S M. The characterization of Fe-rich phases in a high-pressure die cast hypoeutectic aluminum-silicon alloy [J]. Journal of Materials Science & Technology, 2020, 51: 54−62.

[20] MA Si-ming, WANG Yong-sheng, WANG Xiao-ming. The in-situ formation of Al_3Ti reinforcing particulates in an Al−7wt.%Si alloy and their effects on mechanical properties [J]. Journal of Alloys and Compounds, 2019, 792: 365−374.

[21] GAN Jun-qi, HUANG Yu-jian, DU Jun, WEN Cheng, LIU Jing. Synchronous improvement in thermal conductivity and mechanical properties of Al−7Si−0.6Fe−0.5Zn cast alloy by B/La/Sr composite modification [J]. Materials Research Express, 2020, 7: 086501.

[22] LAZARO-NEBREDA J, PATEL J B, FAN Zhong-yun. Improved degassing efficiency and mechanical properties of A356 aluminium alloy castings by high shear melt conditioning (HSMC) technology [J]. Journal of Materials Processing Technology, 2021, 294: 117146.

[23] CAO Yu-dong, CHEN Xiao-hua, WANG Zi-dong, CHEN Kai-xuan, PAN Shi-wen, ZHU Yu-zhi, WANG Yan-lin. Synergistic influence of La and Zr on microstructure and mechanical performance of an Al−Si−Mg alloy at casting state [J]. Journal of Alloys and Compounds, 2022, 902: 163829.

[24] ULUDAG M, ÇETIN R, GEMI L, DISPINAR D. Change in porosity of A356 by holding time and its effect on mechanical properties [J]. Journal of Materials Engineering and Performance, 2018, 27: 5141−5151.

[25] SUN Jian-bo, ZENG Guang-kai, RAO De-wang, WANG Yu-chen, YANG Yi-wang, PAN Li-wen, HU Zhi-liu. Microstructure and tensile properties of a cast eutectic Al−Si−Cu alloy modified by Zr and V [J]. Metals and Materials International, 2021, 27: 5436−5449.

[26] ZHAN Hong-yi, XU Yi-wu, WANG Pan, WANG Jian-feng, LI Jin-ping, ZHANG Le-peng. Effects of magnesium and copper additions on tensile properties of Al−Si−Cr die casting alloy under as-cast and T5 conditions [J]. China Foundry, 2023, 20: 12−22.

[27] VANDERSLUIS E, LOMBARDI A, RAVINDRAN C, BOIS-BROCHU A, CHIESA F, MACKAY R. Factors influencing thermal conductivity and mechanical properties in 319 Al alloy cylinder heads [J]. Materials Science and Engineering A, 2015, 648: 401−411.

[28] CHEN Fei-fan, ZHAO Hai-dong, ZHU Gang, FU Pai-xian, XIA Li-jun. Experimental and numerical analysis of flow behavior and particle distribution in A356/SiC_p composite casting [J]. Experimental Thermal and Fluid Science, 2015, 68: 39−47.

[29] LUMLEY R N, POLMEAR I J, GROOT H, FERRIER J. Thermal characteristics of heat-treated aluminum high-pressure die-castings [J]. Scripta Materialia, 2008, 58: 1006−1009.

[30] SHIN J S, KO S H, KIM K T. Development and characterization of low-silicon cast aluminum alloys for thermal dissipation [J]. Journal of Alloys and Compounds, 2015, 644: 673−686.

[31] ZHANG Cong, DU Yong, LIU Shu-hong, LIU Shao-jun, JIE Wan-qi, SUNDMAN B. Microstructure and thermal conductivity of the as-cast and annealed Al−Cu−Mg−Si alloys in the temperature range from 25 to 400 °C [J]. International Journal of Thermophysics, 2015, 36: 2869−2880.

[32] QI Ming-fan, KANG Yong-lin, TANG Wen-chuan, QIU Quan-quan, LI Bao-shun. Microstructure, mechanical properties and corrosion behavior of Rheo-HPDC a novel Al−8Si−Fe alloy [J]. Materials Letters, 2018, 213: 378−382.

[33] SONG Xin-yue, GAO Min-qiang, YANG Bo-wei, GUAN

Ren-guo. Modification and refinement of Fe-containing phases, mechanical properties and strengthening mechanisms in Al−Fe alloys via Cr alloying and continuous rheo-extrusion [J]. Materials Science and Engineering A, 2022, 850: 143557.

[34] LIU Yan, GAO Min-qiang, FU Ying, LI Wei-rong, YANG Pan, GUAN Ren-guo. Microstructure evolution and solidification behavior of a novel semi-solid alloy slurry prepared by vibrating contraction inclined plate [J]. Metals, 2021, 11: 1810.

[35] CHANG Liang, DING Yu-ming, GUO Bin-xun, DING Jian, XIA Xing-chuan, TANG Ying, LI Chong, SUN Xiao-mian, GUO Jun-jie, SONG Kai-hong, WANG Li-sheng, ZHOU Kai-peng, CHEN Xue-guang, LIU Yong-chang. Modification mechanism and tensile property of Al−9Si−0.4Mg−0.1Cu alloy [J]. Materials Characterization, 2022, 184: 111693.

[36] JI Shou-xun, YANG Wen-chao, GAO Feng, WATSON D, FAN Zhong-yun. Effect of iron on the microstructure and mechanical property of Al−Mg−Si−Mn and Al−Mg−Si diecast alloys [J]. Materials Science and Engineering A, 2013, 564: 130−139.

[37] CAI Qing, MENDIS C L, CHANG I T H, FAN Zhong-yun. Effect of short T6 heat treatment on the microstructure and the mechanical properties of newly developed die-cast Al−Si−Mg−Mn alloys [J]. Materials Science and Engineering A, 2020, 788: 139610.

[38] WANG Yu, GAO Min-qiang, YANG Bo-wei, ZHAO Er-tuan, LIU Feng-guo, GUAN Ren-guo. Microstructural evolution and mechanical property of Al−Mg−Mn alloys with various solidification cooling rates [J]. Materials Characterization, 2022, 184: 111709.

[39] HE Yi, XI Hai-hui, MING Wen-quan, SHAO Qin-qin, SHEN Ruo-han, LAI Yu-xiang, WU Cui-lan, CHEN Jiang-hua. Thermal stability and precipitate microstructures of Al−Si−Mg−Er alloy [J]. Transactions of Nonferrous Metals Society of China, 2021, 31: 1−10.

[40] XIAO Yao, LAN Xin-yue, LU Qiang, DU Yong, LI Kai. In-situ evidence for rotation of Si particles with respect to grains in tensile-deformed Al−Si alloys [J]. Transactions of Nonferrous Metals Society of China, 2023, 33: 1655−1664.

[41] NAMPOOTHIRI J, BALASUNDAR I, RAJ B, MURTY B S, RAVI K R. Porosity alleviation and mechanical property improvement of strontium modified A356 alloy by ultrasonic treatment [J]. Materials Science and Engineering A, 2018, 724: 586−593.

[42] HOU J P, LI R, WANG Q, YU H Y, ZHANG Z J, CHEN Q Y, MA H, WU X M, Li X W, ZHANG Z F. Three principles for preparing Al wire with high strength and high electrical conductivity [J]. Journal of Materials Science & Technology, 2019, 35: 742−751.

Sr、Mn 合金化对铸态 Al−Si−Fe−Mg−Cu 合金显微组织与综合性能的影响

孟拴成[1,2]，杨 莉[1]，高民强[1,3]，李军文[1]，管仁国[1,3]

1. 大连交通大学 辽宁省轻质金属材料近净成形重点实验室，大连 116028；
2. 东北大学 材料科学与工程学院，沈阳 110819；
3. 大连交通大学 连续挤压教育部工程研究中心，大连 116028

摘 要：为了制备综合性能优异的 Al−Si−Fe−Mg−Cu 合金，采用 Sr 和 Mn 元素对共晶 Si 和富 Fe 第二相进行改性。结果表明，当 Sr 含量从 0 增加至 0.02%(质量分数)，共晶 Si 形貌由粗大片层状变为了细小纤维状。然而，由于 Sr 添加易引起孔隙率上升，Sr 含量为 0.03%(质量分数)的铸态 Al−Si−Fe−Mg−Cu 合金的力学和热导率下降。在优化 Sr 含量基础之上，加入 Mn 进一步调控铸态合金的性能。当 Mn 含量由 0.2%增加至 0.6%(质量分数)，针状 β-Al_5FeSi 相转变为汉字状 α-$Al_{15}(Fe,Mn)_3Si_2$ 相，合金力学性能先升高后降低。由于 Mn 原子的固溶，合金热导率降低。相比之下，添加 0.02% Sr 和 0.4% Mn(质量分数)的 Al−Si−Fe−Mg−Cu−Sr 合金表现出优异的综合性能，其热导率为 168.5 W/(m·K)，抗拉强度为 201.9 MPa，屈服强度为 115.3 MPa，伸长率为 9.0%。

关键词：Al−Si 合金；变质处理；第二相；力学性能；热导率

(Edited by Bing YANG)